Original Article

Institution of MECHANICAL ENGINEERS

Journal of MECHANICAL ENGINEERING SCIENCE

Proc IMechE Part C:
J Mechanical Engineering Science
2021, Vol. 235(20) 4768–4783

DOI: 10.1177/0954406220948910
journals.sagepub.com/home/pic

SAGE

Dual-mass electromagnetic energy harvesting from galloping oscillations and base excitation

Danilo Karličić[1,2], Milan Cajić[2] and Sondipon Adhikari[1]

Abstract

This paper investigates electromagnetic energy harvesting based on vibration energy extraction from the vibration of a bluff body elastically connected with an additional nonlinear oscillator and subjected to fluid flow and base excitation. The mechanical part is modeled as a system of two coupled oscillators where a combination of harmonic base excitation and fluid forces leads to a steady-state regime. The electromagnetic generator as part of the harvesting device is represented by the equivalent electrical circuit with power dissipated at an electrical load resistance. The mathematical model is based on a set of two coupled nonlinear ordinary differential equations considering the transverse displacement of a bluff body, additional nonlinear oscillator, and currents induced in the electromagnetic generator. By introducing the incremental harmonic balance and continuation methods nonlinear periodic responses are investigated and complex dynamic behavior presented through corresponding response diagrams. The results indicate that for some values of system parameters multiple periodic solutions appear in the form of loops and hysteresis. Finally, the average power of proposed energy harvester is given in time history diagrams for different values of nonlinear stiffness parameter and velocity of fluid flow.

Keywords

Fluid induced vibration, energy harvester, dual mass, incremental harmonic balance method, continuation technique, periodic response

Date received: 31 October 2019; accepted: 20 July 2020

Introduction

The problem of flow-induced vibration in structural dynamics has received significant attention from the scientific community in the last few decades due to wide engineering applications in many fields such as civil engineering, aerospace engineering, and power technology.[1] From the viewpoint of energy harvesting application, fluid-induced vibration phenomena can be used for supplying small sensors and microelectronic devices placed in modern bridges, tall buildings, and aerospace structures.[2] On the other hand, fluid-induced vibration can cause many problems in engineering structures due to nonlinear phenomena such as vortex-induced vibration, galloping, and flutter. These flow-induced instabilities can excite structures in such a way that the amplitude vibration of structures grows over time leading to failure. The main question that arises from these facts is whether it is possible to control vibration amplitudes and to harvest a part of the mechanical energy of the oscillating bluff body by using some of the well-known methodologies based on the electromagnetic, piezoelectric and electrostatic principles[3] and introducing additional oscillators. In scientific literature, the most practiced methodology for converting mechanical energy induced by flow instability phenomena into electric power is based on the piezoelectric effect. The collection of papers proposed by Abdelkefi et al.,[4–6] illustrates unique solutions of using piezoelectric energy harvesting principles in energy scavenging from a bluff body in cross-flow. Moreover, Dai et al.[7] presented the energy harvesting principle based on piezoelectric patches mounted on a beam inside a bluff body. They derived an analytical model in the form of a set of ordinary differential equations by using the Euler–Lagrange principle

[1]College of Engineering, Swansea University, Swansea, UK
[2]Mathematical Institute of the Serbian Academy of Science and Art, Belgrade, Serbia

Corresponding author:
Danilo Karličić, Swansea University College of Engineering, Bay Campus, Fabian Way, Crymlyn Burrows, Swansea SA2 8PP, UK.
Email: danilo.karlicic@swansea.ac.uk

and Galerkin method. Furthermore, in Dai et al.[8] the authors have shown another application of piezoelectric effect in energy harvesting using a base motion for excitation of a multi-layered piezoelectric cantilever beam with a circular cylinder tip mass attached to its free end and subjected to uniform airflow.

Electromagnetic energy harvesters based on fluid-induced vibration of structures are analyzed in a small number of studies. In Dai et al.,[9] the authors have analyzed converting mechanical energy of a bluff-body, caused by galloping oscillations, into electrical energy by using an electromagnetic transducer. Vicente-Ludlam et al.[10] presented an analytical study for the electro-fluid-elastic model of electromagnetic energy harvesting from transverse galloping. The authors derived closed-form expressions for optimal electric load, which leads to maximal harvested power for assumed steady-state motion. Moreover, the nonlinear model of galloping energy harvester based on electromagnetic generator attached to a beam with a tip body is studied in Dai et al.[11] By introducing the reduced-order model, the authors determined the optimal configuration of energy harvesting according to the system parameters. In Pennisi et al.,[12] the authors proposed a practical application of electromagnetic energy harvester based on the double-mass system connected by two strings and excited by base motion. The authors have experimentally demonstrated the targeted energy transfer from a primary structure to nonlinear energy sink (NES) as well as a strongly modulated response.

The special class of energy harvesting devices that are introduced in aerospace applications for energy scavenging from oscillating airfoils are presented in Liu and Gao[13] and De Marqui and Erturk.[14] In Dias et al.[15] the authors introduced combined piezoelectric and electromagnetic induction energy harvesters based on three degrees of freedom models of airfoil subjected to vortex-induced vibration. By using numerical methods, the authors have analyzed the effects of aeroelastic parameters and load resistance on total power generation. Bibo and Daqaq[16] proposed the nonlinear piezo-aeroelastic energy harvester subjected to combined base excitation and an aerodynamic load of a rigid airfoil. The authors applied the center manifold reduction to reduce the model into one nonlinear differential equation and then introduced normal form theory to study a slow modulation of response amplitude and phase near flutter instability. More on this subject of energy harvesters based on flow-induced vibration one can find in Daqaq et al.[17]

In order to control vibration amplitude of a primary structure the nonlinear attachment known as NES is introduced, where energy is transferred from a primary structure to NES and dissipated through weak damping as shown in Vakakis et al.[18,19] A general model of the NES system is composed of a light additional mass connect to a primary structure through a nonlinear spring and weak damper.[20] The application of NES in vibration suppression is analyzed in many papers. In the literature, special attention is devoted to the suppression of flow-induced vibration of structures.[21,22]

Dai et al.[23,24] introduced the passive nonlinear energy sink placed into the bluff body in order to control galloping and vortex-induced vibration. The authors determined the coupled frequency and galloping speed based on linear analysis and then applied the nonlinear normal form theory to find instability types and responses of the system near the bifurcation. Moreover, in Dai et al.[24] the authors used the linear and nonlinear analysis and direct numerical simulation method to show the influence of NES in reducing the vibration amplitude of a primary structure subjected to vortex-induced vibration. However, models based on the combination of energy harvesting and nonlinear energy sink are analyzed mostly for base excitation problems.[25,26] From the practical point of view, this model is important in cases where NES is introduced to control vibration amplitudes and at the same time to convert mechanical energy to electrical power for the supply of sensors or other microelectronic devices. On the other hand, the dual-mass system can be applied to amplify extracted power, which leads to more efficient energy harvesting. Tang and Zuo[27] proposed such kind of dual-mass system for energy harvesting purposes and investigated the effects of additional masses on piezoelectric energy harvesting device. They have demonstrated increased efficiency of dual mass concept on the harvested power. Moreover, Nishi[28] introduced this dual-mass concept for energy harvesting from vortex-induced vibration. The authors determined approximate analytical solutions for the presented system to show the benefits of a dual-mass system with respect to the single-mass one. Furthermore, Vicente-Ludlam et al.[29] studied galloping oscillations and the influence of fluid flow on the dual-mass system. The authors introduced a harmonic balance method to investigate the dynamic response of different mass-spring-damper configurations and the effects of fluid flow on the energy harvesting efficiency. To summarize, it can be asserted that energy harvesting devices based on dual-mass models with nonlinear connections in-between and subjected to base excitation and galloping oscillations are not yet investigated and presented in the scientific literature. It should be noted that in the present study, a simplified two-degree of freedom system based on the lumped-parameter model is proposed with the electromagnetic generator represented by an equivalent electric circuit. However, large-scale models analyzed by FEM and experimental techniques one can find in Refs.[42–44]

The aim of this communication is to report a dual-mass model of energy harvester with potential vibration control capabilities, which is based on a bluff

body subjected to simultaneous transverse cross-flow and base excitation. However, in this study, the primary focus will be on investigation of the influence of introduced nonlinearity on energy harvesting (EH) performance for the presented dual-mass system developed in Vicente-Ludlam et al.[29] The reason for introducing the additional nonlinear oscillator is an amplification of the vibration response in such a way that the EH device can extract larger portions of mechanical energy and convert it into electric power for a wide range of excitation frequencies. At the same time, the additional nonlinear oscillator can reduce the response resonant amplitude of the primary system i.e. to be used as NES.[23,24] The electromagnetic generator is attached to the primary structure of the system, where the relative motion between the oscillating magnet and fixed coil leads to electric current induction. The mechanical part of the proposed system is based on the base excited dual-mass system, where internal mass is connected to the primary structure through a nonlinear spring and damper. The set of three nonlinear differential equations corresponding to the proposed electromechanical model, with two of them describing mechanical displacements of a bluff body and nonlinear oscillator, while the third one corresponds to an equivalent electric circuit of the electromagnetic generator. The fluid force is introduced through galloping oscillation phenomena with a corresponding mathematical model adopted in the form of cubic polynomial approximation.[5,10,23] In order to determine frequency and force responses of the proposed system excited by a combination of base excitation and cross-flow, the incremental harmonic balance (IHB) and continuation methods are applied. The presented methodology can detect different nonlinear phenomena such as jumps and loops that are generated by the introduced additional nonlinear oscillator. Moreover, by considering time history diagrams the average power of the proposed system is estimated for different values of the nonlinear stiffness parameter and flow speed. The obtained results revealed that the presented dual-mass system can significantly improve the efficiency of the energy harvesting device.

Mathematical model of the dual-mass energy harvester

The aeroelastic energy harvester (EH) excited by base motion and with the attached nonlinear oscillator is considered. The electromagnetic EH model is represented by the dual-mass system coupled with nonlinear spring and linear damper, where the primary mass m_1^* is excited by external harmonic base excitation through the linear spring of stiffness k_1 and damper with the viscous coefficient c_1, as shown in Figure 1. The electromagnetic generator is represented by the oscillating magnet linked to a primary structure that oscillates relative to the coil and producing electricity which is dissipated by the electric resistive load R_L. The primary structure oscillates in x direction, transverse to the incident flow, which causes the galloping oscillations. Moreover, the general model of an additional oscillator is modeled as a nonlinear attachment composed of attached mass m_2, nonlinear spring k_2 and linear damping c_2. The additional nonlinear oscillator oscillates in x direction, inside of the primary structure.

According to Refs.,[23,30] the galloping phenomena appear in the system when the total electromechanical damping changes the sign from positive to negative value because of the aerodynamic force. Moreover, when the total value of the system's electromechanical damping is equal to zero, the flow speed corresponding to one type of instability phenomena leads to critical or galloping speed. Furthermore, the instability rises from galloping phenomena is Hopf bifurcations, while the values of flow speed larger than the critical galloping speed lead to supercritical Hopf bifurcations and limit cycle oscillations. As stated in Javed et al.,[30] by performing the linear analysis one can find eigenvalues of a system, where for particular values of the electrical load resistance there are corresponding values of the galloping speed. The focus of this study is to examine a nonlinear periodic response of the electromagnetic energy harvester with attached nonlinear oscillator subjected to base excitation and fluid flow, where the influence of flow speed is larger than the critical galloping speed.

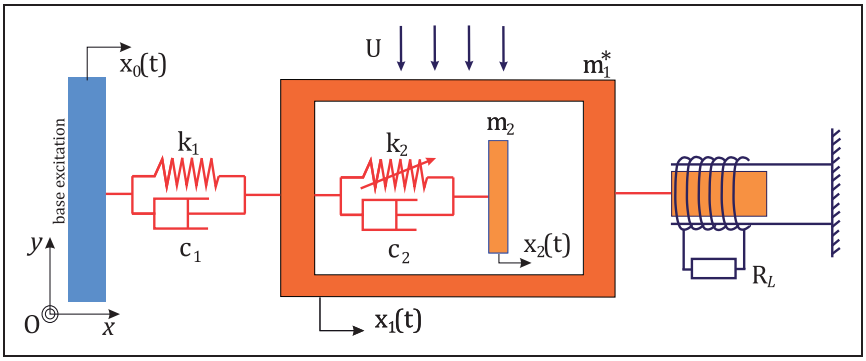

Figure 1. Simplified model of a base excited aeroelastic energy harvester with an additional nonlinear oscillator.

The governing equations of motion of the electromagnetic energy harvester having an additional nonlinear oscillator and subjected to external base excitation and fluid flow are given in the following form

$$(m_1 - m_2)\frac{d^2x_1}{dt^2} + k_1(x_1 - x_0) + c_1\left(\frac{dx_1}{dt} - \frac{dx_0}{dt}\right) + k_2(x_1 - x_2)^3 + c_2\left(\frac{dx_1}{dt} - \frac{dx_2}{dt}\right) = F_U + F_{emf} \tag{1a}$$

$$m_2\frac{d^2x_2}{dt^2} + k_2(x_2 - x_1)^3 + c_2\left(\frac{dx_2}{dt} - \frac{dx_1}{dt}\right) = 0 \tag{1b}$$

$$(R_L + R_C)i + L_C\frac{di}{dt} = V_{emf} \tag{1c}$$

where F_U represents the galloping force, F_{emf} is introduced electromagnetic force and V_{emf} is the relationship between the amplitude of the velocity and electromotive force, defined as

$$F_U = \frac{1}{2}\rho U^2 D\left[\frac{a_1}{U}\frac{dx_1}{dt} + \frac{a_3}{U^3}\left(\frac{dx_1}{dt}\right)^3\right] \tag{2a}$$

$$F_{emf} = -k_E i \tag{2b}$$

$$V_{emf} = k_E\frac{dx_1}{dt} \tag{2c}$$

in which ρ is the fluid density, D is the effective diameter of the bluff body and U is the speed of fluid flow.[10,29] The coefficients a_1 and a_3 are determined based on the experiments.[10,31]

In this study, we assume that the base is harmonically excited as $x_0(t) = F_0\cos\Omega t$, where F_0 is the amplitude and Ω is the excitation frequency. Moreover, the reduced mass of the bluff body is taken as $m_1 - m_2$, were ensuring no mass addition due to additional nonlinear oscillator. The third equation in the system of equation (1) represents the mathematical model of the equivalent electric circuit of the electromagnetic generator as defined in Refs.[10,32] where R_L is the resistance of the load connected to the generator, R_C is the internal resistance of the coil, L_C is its inductance, k_E is the electromechanical coupling constant and i is the induced current in the coil.

The equations of motion are obtained by scaling the length and using the diameter of the bluff body to define the dimensionless mechanical degree-of-freedom $x_1 = D\bar{x}_1$ and $x_2 = D\bar{x}_2$, and introducing a new time scale $\tau = \Omega t$, where the system of equation (1) now takes a new dimensionless form as

$$(1-\Gamma)\left(\frac{\Omega}{\omega_N}\right)^2\frac{d^2\bar{x}_1}{d\tau^2} + \bar{x}_1 + 2\zeta\left(\frac{\Omega}{\omega_N}\right)\frac{d\bar{x}_1}{d\tau} + \alpha(\bar{x}_1 - \bar{x}_2)^3 + \beta\left(\frac{\Omega}{\omega_N}\right)\left(\frac{d\bar{x}_1}{d\tau} - \frac{d\bar{x}_2}{d\tau}\right) = \frac{\bar{U}}{2m^*}\left(\frac{\Omega}{\omega_N}\right)\left[a_1\frac{d\bar{x}_1}{d\tau} + \frac{a_3}{\bar{U}^2}\left(\frac{\Omega}{\omega_N}\right)^2\left(\frac{d\bar{x}_1}{d\tau}\right)^3\right] - I + f\cos(\tau) - 2\zeta f\left(\frac{\Omega}{\omega_N}\right)\sin(\tau) \tag{2d}$$

$$\left(\frac{\Omega}{\omega_N}\right)^2\frac{d^2\bar{x}_2}{d\tau^2} + \xi\alpha(\bar{x}_2 - \bar{x}_1)^3 + \xi\beta\left(\frac{\Omega}{\omega_N}\right)\left(\frac{d\bar{x}_2}{d\tau} - \frac{d\bar{x}_1}{d\tau}\right) = 0 \tag{2e}$$

$$I + \gamma\left(\frac{\Omega}{\omega_N}\right)\frac{dI}{d\tau} = 2\zeta_E\left(\frac{\Omega}{\omega_N}\right)\frac{d\bar{x}_1}{d\tau} \tag{2f}$$

where new parameters are defined as

$$\omega_N = \sqrt{k_1/m_1}, \quad \Gamma = \frac{m_2}{m_1} = \frac{1}{\xi}, \quad \zeta = \frac{c_1}{2\sqrt{k_1 m_1}}, \quad f = \frac{F_0}{D}, \quad m^* = \frac{m_1}{\rho D^2}, \quad \bar{U} = \frac{U}{D\omega_N},$$

$$\alpha = \frac{D^2k_2}{m_1\omega_N^2}, \quad \beta = \frac{c_2}{\sqrt{k_1 m_1}}, \quad I_C = \frac{m_1\omega_N^2 D}{k_E}, \quad I = \frac{i}{I_C}, \quad \gamma = \frac{L_C\omega_N}{(R_L + R_C)}, \quad \zeta_E = \frac{k_E D\omega_N}{2(R_L + R_C)I_C}.$$

The incremental harmonic balance method

To determine the periodic responses of the electromagnetic EH system from Figure 1, the IHB method is introduced. The semi-analytical solution of the system of nonlinear ordinary differential equations is obtained in the form of the Fourier series. Moreover, the frequency and force responses are traced by implementing the IHB and continuation methods. Due to its generality, IHB method was applied in many other engineering problems from structural dynamics,[33] analysis of MEMS,[34] vibration suppression using the nonlinear energy sink[35] and vehicle dynamics.[36] In this study, the main interest is on tracing the frequency-amplitude and force-amplitude curves of the electromagnetic EH subjected to base excitation and fluid flow and estimating the EH power for different values of the amplitude of external base excitation and speed of fluid flow. In the following, we will provide more details on how to trace frequency response curves by using the same methodology, which will

enable us to trace the response of any other parameter of the system.

We introduce the incremental relations for $\bar{x}_1, \bar{x}_2$, I and Ω in the following forms

$$\begin{aligned}&\bar{x}_1(\tau) = \bar{x}_{10}(\tau) + \Delta\bar{x}_1(\tau),\\ &\bar{x}_2(\tau) = \bar{x}_{20}(\tau) + \Delta\bar{x}_2(\tau), \quad I(\tau) = I_0(\tau) + \Delta I(\tau),\\ &\Omega = \Omega_0 + \Delta\Omega\end{aligned} \tag{3}$$

where $\bar{x}_{10}, \bar{x}_{20}$, I_0 and Ω_0 denotes a known vibration state, and $\Delta\bar{x}_1$, $\Delta\bar{x}_2$, ΔI and $\Delta\Omega$ are the corresponding increments of the displacements x_1 and $\bar{x}_2$, electrical current I and excitation frequency Ω. The periodic solutions of $\bar{x}_1, \bar{x}_2$ and I is assumed in the form of Fourier series with only odd terms, where the functions $(\bar{x}_{10}, \Delta\bar{x}_1), (\bar{x}_{20}, \Delta\bar{x}_2)$ and $(I_0, \Delta I)$ can be taken in the following form

$$\bar{x}_{10}(\tau) = \sum_{k=1}^{N_h} \left\{a_{1k}\cos(k\tau) + b_{1k}\sin(k\tau)\right\} = \boldsymbol{C}\cdot\boldsymbol{A}_1 \tag{4a}$$

$$\Delta\bar{x}_1(\tau) = \sum_{k=1}^{N_h} \left\{\Delta a_{1k}\cos(k\tau) + \Delta b_{1k}\sin(k\tau)\right\} = \boldsymbol{C}\cdot\Delta\boldsymbol{A}_1 \tag{4b}$$

$$\bar{x}_{20}(\tau) = \sum_{k=1}^{N_h} \left\{a_{2k}\cos(k\tau) + b_{2k}\sin(k\tau)\right\} = \boldsymbol{C}\cdot\boldsymbol{A}_2 \tag{4c}$$

$$\begin{aligned}\Delta\bar{x}_2(\tau) &= \sum_{k=1}^{N_h} \left\{\Delta a_{2k}\cos(k\tau) + \Delta b_{2k}\sin(k\tau)\right\}\\ &= \boldsymbol{C}\cdot\Delta\boldsymbol{A}_2\end{aligned} \tag{4d}$$

$$I_0(\tau) = \sum_{k=1}^{N_h} \left\{a_{3k}\cos(k\tau) + b_{3k}\sin(k\tau)\right\} = \boldsymbol{C}\cdot\boldsymbol{A}_3 \tag{4e}$$

$$\Delta I(\tau) = \sum_{k=1}^{N_h} \left\{\Delta a_{3k}\cos(k\tau) + \Delta b_{3k}\sin(k\tau)\right\} = \boldsymbol{C}\cdot\Delta\boldsymbol{A}_3 \tag{4f}$$

where

$$\begin{aligned}\boldsymbol{C} = [&\cos\tau \quad \cos3\tau \quad \cos5\tau \ldots\\ &\cos N_h\tau \quad \sin\tau \quad \sin3\tau\,\sin5\tau \ldots \sin N_h\tau]\end{aligned} \tag{5}$$

$$\boldsymbol{A}_{ip} = [a_{i1} \quad a_{i3} \quad a_{i5} \ldots a_{iN_h} \quad b_{i1} \quad b_{i3} \quad b_{i5} \ldots b_{iN_h}]^T$$

$$\begin{aligned}\Delta\boldsymbol{A}_{ip} = [&\Delta a_{i1} \quad \Delta a_{i3} \quad \Delta a_{i5} \ldots \Delta a_{iN_h}\\ &\Delta b_{i1} \quad \Delta b_{i3} \quad \Delta b_{i5} \ldots \Delta b_{iN_h}]^T, i = 1,2,3\end{aligned}$$

Introducing the equations (3) and (4) into equation (2), and applying the Galerkin procedure in order to eliminate parameter τ with neglected higher-order terms, we can get the following system of algebraic equations

$$\begin{aligned}&\begin{bmatrix}\boldsymbol{K}_{11} & \boldsymbol{K}_{12} & \boldsymbol{K}_{13}\\ \boldsymbol{K}_{21} & \boldsymbol{K}_{22} & 0\\ \boldsymbol{K}_{31} & 0 & \boldsymbol{K}_{33}\end{bmatrix}\begin{Bmatrix}\Delta\boldsymbol{A}_1\\ \Delta\boldsymbol{A}_2\\ \Delta\boldsymbol{A}_3\end{Bmatrix}\\ &= \begin{Bmatrix}\tilde{\boldsymbol{F}}_1\\ 0\\ 0\end{Bmatrix} + \begin{bmatrix}\boldsymbol{R}_{11} & \boldsymbol{R}_{12} & \boldsymbol{R}_{13}\\ \boldsymbol{R}_{21} & \boldsymbol{R}_{22} & 0\\ \boldsymbol{R}_{31} & 0 & \boldsymbol{R}_{33}\end{bmatrix}\begin{Bmatrix}\boldsymbol{A}_1\\ \boldsymbol{A}_2\\ \boldsymbol{A}_3\end{Bmatrix}\\ &\quad + \begin{Bmatrix}\tilde{\boldsymbol{V}}_1\\ \tilde{\boldsymbol{V}}_2\\ \tilde{\boldsymbol{V}}_3\end{Bmatrix}\Delta\Omega\end{aligned} \tag{6a}$$

or in the simplified form as

$$\boldsymbol{K}\Delta\boldsymbol{A} = \boldsymbol{R} + \tilde{\boldsymbol{V}}\Delta\Omega \tag{6b}$$

where elements of matrix $\boldsymbol{K}$ and vector $\boldsymbol{R}$ are given as

$$\begin{aligned}\boldsymbol{K}_{11} = \int_0^{2\pi}\Bigg[&(1-\Gamma)\left(\frac{\Omega_0}{\omega_N}\right)^2\boldsymbol{C}^T\frac{d^2\boldsymbol{C}}{d\tau^2} + \boldsymbol{C}^T\boldsymbol{C} + 2\zeta\left(\frac{\Omega_0}{\omega_N}\right)\boldsymbol{C}^T\frac{d\boldsymbol{C}}{d\tau}\\ &+ 3\alpha\left(\bar{x}_{10}^2 - 2\bar{x}_{10}\bar{x}_{20} + \bar{x}_{20}^2\right)\boldsymbol{C}^T\boldsymbol{C}\\ &+ \beta\left(\frac{\Omega_0}{\omega_N}\right)\boldsymbol{C}^T\frac{d\boldsymbol{C}}{d\tau} - \frac{\bar{U}a_1}{2m^*}\left(\frac{\Omega_0}{\omega_N}\right)\boldsymbol{C}^T\frac{d\boldsymbol{C}}{d\tau}\\ &- \frac{3a_3}{2m^*\bar{U}}\left(\frac{\Omega_0}{\omega_N}\right)^3\left(\frac{d\bar{x}_1}{d\tau}\right)^2\boldsymbol{C}^T\frac{d\boldsymbol{C}}{d\tau}\Bigg]\mathrm{d}\tau\end{aligned}$$

$$\boldsymbol{K}_{12} = \int_0^{2\pi}\left[-3\alpha\left(\bar{x}_{10}^2 - 2\bar{x}_{10}\bar{x}_{20} + \bar{x}_{20}^2\right)\boldsymbol{C}^T\boldsymbol{C} - \beta\left(\frac{\Omega_0}{\omega_N}\right)\boldsymbol{C}^T\frac{d\boldsymbol{C}}{d\tau}\right]\mathrm{d}\tau$$

$$\boldsymbol{K}_{13} = \int_0^{2\pi}[\boldsymbol{C}^T\boldsymbol{C}]\mathrm{d}\tau$$

$$\boldsymbol{K}_{21} = \int_0^{2\pi}\left[-3\xi\alpha\left(\bar{x}_{20}^2 - 2\bar{x}_{10}\bar{x}_{20} + \bar{x}_{10}^2\right)\boldsymbol{C}^T\boldsymbol{C} - \xi\beta\left(\frac{\Omega_0}{\omega_N}\right)\boldsymbol{C}^T\frac{d\boldsymbol{C}}{d\tau}\right]\mathrm{d}\tau$$

$$\begin{aligned}\boldsymbol{K}_{22} = \int_0^{2\pi}\Bigg[&\left(\frac{\Omega_0}{\omega_N}\right)^2\boldsymbol{C}^T\frac{d^2\boldsymbol{C}}{d\tau^2} + 3\xi\alpha\left(\bar{x}_{20}^2 - 2\bar{x}_{10}\bar{x}_{20} + \bar{x}_{10}^2\right)\boldsymbol{C}^T\boldsymbol{C}\\ &+ \xi\beta\left(\frac{\Omega_0}{\omega_N}\right)\boldsymbol{C}^T\frac{d\boldsymbol{C}}{d\tau}\Bigg]\mathrm{d}\tau\end{aligned}$$

$$\boldsymbol{K}_{31} = \int_0^{2\pi}\left[-2\zeta_E\left(\frac{\Omega_0}{\omega_N}\right)\boldsymbol{C}^T\frac{d\boldsymbol{C}}{d\tau}\right]\mathrm{d}\tau$$

$$\boldsymbol{K}_{33} = \int_0^{2\pi}\left[\boldsymbol{C}^T\boldsymbol{C} + \gamma\left(\frac{\Omega_0}{\omega_N}\right)\boldsymbol{C}^T\frac{d\boldsymbol{C}}{d\tau}\right]\mathrm{d}\tau \tag{7a}$$

$$\tilde{\boldsymbol{F}}_1 = \int_0^{2\pi}\left[f\boldsymbol{C}^T\cos(\tau) - 2\zeta\left(\frac{\Omega_0}{\omega_N}\right)f\boldsymbol{C}^T\sin(\tau)\right]\mathrm{d}\tau \tag{7b}$$

$$\boldsymbol{R}_{11} = -\int_0^{2\pi} \Bigg[(1-\Gamma)\left(\frac{\Omega_0}{\omega_N}\right)^2 \boldsymbol{C}^{\boldsymbol{T}} \frac{d^2\boldsymbol{C}}{d\tau^2} + \boldsymbol{C}^{\boldsymbol{T}}\boldsymbol{C} + 2\zeta\left(\frac{\Omega_0}{\omega_N}\right)\boldsymbol{C}^{\boldsymbol{T}} \frac{d\boldsymbol{C}}{d\tau} + \alpha\left(\bar{x}_{10}^2 - 3\bar{x}_{10}\bar{x}_{20}\right)\boldsymbol{C}^{\boldsymbol{T}}\boldsymbol{C} + \beta\left(\frac{\Omega_0}{\omega_N}\right)\boldsymbol{C}^{\boldsymbol{T}} \frac{d\boldsymbol{C}}{d\tau} - \frac{\bar{U}a_1}{2m^*}\left(\frac{\Omega_0}{\omega_N}\right)\boldsymbol{C}^{\boldsymbol{T}} \frac{d\boldsymbol{C}}{d\tau} - \frac{a_3}{2m^*\bar{U}}\left(\frac{\Omega_0}{\omega_N}\right)^3 \left(\frac{d\bar{x}_1}{d\tau}\right)^2 \boldsymbol{C}^{\boldsymbol{T}} \frac{d\boldsymbol{C}}{d\tau} \Bigg] \mathrm{d}\tau$$

$$\boldsymbol{R}_{12} = -\int_0^{2\pi} \left[\alpha\left(3\bar{x}_{10}\bar{x}_{20} - \bar{x}_{20}^2\right)\boldsymbol{C}^{\boldsymbol{T}}\boldsymbol{C} - \beta\left(\frac{\Omega_0}{\omega_N}\right)\boldsymbol{C}^{\boldsymbol{T}} \frac{d\boldsymbol{C}}{d\tau} \right] \mathrm{d}\tau$$

$$\boldsymbol{R}_{13} = -\int_0^{2\pi} [\mathbf{C}^{\mathbf{T}}\mathbf{C}]\mathbf{d}\boldsymbol{\tau}$$

$$\boldsymbol{R}_{21} = -\int_0^{2\pi} \left[\xi\alpha\left(3\bar{x}_{10}\bar{x}_{20} - \bar{x}_{10}^2\right)\boldsymbol{C}^{\boldsymbol{T}}\boldsymbol{C} - \xi\beta\left(\frac{\Omega_0}{\omega_N}\right)\boldsymbol{C}^{\boldsymbol{T}} \frac{d\boldsymbol{C}}{d\tau} \right] \mathrm{d}\tau$$

$$\boldsymbol{R}_{22} = -\int_0^{2\pi} \left[\left(\frac{\Omega_0}{\omega_N}\right)^2 \boldsymbol{C}^{\boldsymbol{T}} \frac{d^2\boldsymbol{C}}{d\tau^2} + \xi\alpha\left(\bar{x}_{20}^2 - 3\bar{x}_{10}\bar{x}_{20}\right)\boldsymbol{C}^{\boldsymbol{T}}\boldsymbol{C} + \xi\beta\left(\frac{\Omega_0}{\omega_N}\right)\boldsymbol{C}^{\boldsymbol{T}} \frac{d\boldsymbol{C}}{d\tau} \right] d\tau$$

$$\boldsymbol{R}_{31} = -\int_0^{2\pi} \left[-2\zeta_E\left(\frac{\Omega_0}{\omega_N}\right)\boldsymbol{C}^{\boldsymbol{T}} \frac{d\boldsymbol{C}}{d\tau} \right] \mathrm{d}\tau$$

$$\boldsymbol{R}_{33} = -\int_0^{2\pi} \left[\boldsymbol{C}^{\boldsymbol{T}}\boldsymbol{C} + \gamma\left(\frac{\Omega_0}{\omega_N}\right)\boldsymbol{C}^{\boldsymbol{T}} \frac{d\boldsymbol{C}}{d\tau} \right] \mathrm{d}\tau \tag{7c}$$

The vector $\tilde{\boldsymbol{V}}$ is defined as

$$\tilde{\boldsymbol{V}}_1 = \boldsymbol{V}_{11}\boldsymbol{A}_1 + \boldsymbol{V}_{12}\boldsymbol{A}_2 + \tilde{\boldsymbol{f}}_1,$$

$$\tilde{\boldsymbol{V}}_2 = \boldsymbol{V}_{21}\boldsymbol{A}_1 + \boldsymbol{V}_{22}\boldsymbol{A}_2,$$

$$\tilde{\boldsymbol{V}}_3 = \boldsymbol{V}_{31}\boldsymbol{A}_1 + \boldsymbol{V}_{33}\boldsymbol{A}_3 \tag{7d}$$

where matrices are determined as

$$\boldsymbol{V}_{11} = \int_0^{2\pi} \Bigg[-(1-\Gamma)\left(\frac{2\Omega_0}{\omega_N^2}\right)\boldsymbol{C}^{\boldsymbol{T}} \frac{d^2\boldsymbol{C}}{d\tau^2} - 2\left(\frac{\zeta}{\omega_N}\right)\boldsymbol{C}^{\boldsymbol{T}} \frac{d\boldsymbol{C}}{d\tau} - \left(\frac{\beta}{\omega_N}\right)\boldsymbol{C}^{\boldsymbol{T}} \frac{d\boldsymbol{C}}{d\tau} + \frac{\bar{U}a_1}{2\omega_N m^*}\boldsymbol{C}^{\boldsymbol{T}} \frac{d\boldsymbol{C}}{d\tau} + \frac{3a_3\Omega_0^2}{2m^*\bar{U}\omega_N^3}\left(\frac{d\bar{x}_1}{d\tau}\right)^2 \boldsymbol{C}^{\boldsymbol{T}} \frac{d\boldsymbol{C}}{d\tau} \Bigg] \mathrm{d}\tau,$$

$$\boldsymbol{V}_{12} = \int_0^{2\pi} \left[\left(\frac{\beta}{\omega_N}\right)\boldsymbol{C}^{\boldsymbol{T}} \frac{d\boldsymbol{C}}{d\tau} \right] \mathrm{d}\tau,$$

$$\tilde{\boldsymbol{f}}_1 = \int_0^{2\pi} \left[-\left(\frac{2\zeta f}{\omega_N}\right)\boldsymbol{C}^{\boldsymbol{T}} \sin(\tau) \right] \mathrm{d}\tau$$

$$\boldsymbol{V}_{21} = \int_0^{2\pi} \left[\left(\frac{\xi\beta}{\omega_N}\right)\boldsymbol{C}^{\boldsymbol{T}} \frac{d\boldsymbol{C}}{d\tau} \right] d\tau,$$

$$\boldsymbol{V}_{22} = \int_0^{2\pi} \left[-\left(\frac{2\Omega_0}{\omega_N^2}\right)\boldsymbol{C}^{\boldsymbol{T}} \frac{d^2\boldsymbol{C}}{d\tau^2} - \left(\frac{\xi\beta}{\omega_N}\right)\boldsymbol{C}^{\boldsymbol{T}} \frac{d\boldsymbol{C}}{d\tau} \right]$$

$$\boldsymbol{V}_{31} = \int_0^{2\pi} \left[\left(\frac{2\zeta_E}{\omega_N}\right)\boldsymbol{C}^{\boldsymbol{T}} \frac{d\boldsymbol{C}}{d\tau} \right] d\tau,$$

$$\boldsymbol{V}_{33} = \int_0^{2\pi} \left[-\left(\frac{\gamma}{\omega_N}\right)\boldsymbol{C}^{\boldsymbol{T}} \frac{d\boldsymbol{C}}{d\tau} \right] d\tau \tag{7e}$$

By using the same methodology, it is possible to analyze the periodic response of the system by incrementing any other system parameters and formulating the system of incremental equations as given for the frequency response (equation (6)). In the case when the force amplitude f is incremented parameter $f = f_0 + \Delta f$, the force amplitude response curves can be traced. Inserting incremental equations of the amplitude of external force and corresponding displacements from equations (3) and (4) into equation (2), the algebraic equations takes a new form

$$\begin{bmatrix} \boldsymbol{K}_{11} & \boldsymbol{K}_{12} & \boldsymbol{K}_{13} \\ \boldsymbol{K}_{21} & \boldsymbol{K}_{22} & 0 \\ \boldsymbol{K}_{31} & 0 & \boldsymbol{K}_{33} \end{bmatrix} \begin{Bmatrix} \Delta\boldsymbol{A}_1 \\ \Delta\boldsymbol{A}_2 \\ \Delta\boldsymbol{A}_3 \end{Bmatrix} = \begin{Bmatrix} \tilde{\boldsymbol{F}}_1 \\ 0 \\ 0 \end{Bmatrix} + \begin{bmatrix} \boldsymbol{R}_{11} & \boldsymbol{R}_{12} & \boldsymbol{R}_{13} \\ \boldsymbol{R}_{21} & \boldsymbol{R}_{22} & 0 \\ \boldsymbol{R}_{31} & 0 & \boldsymbol{R}_{33} \end{bmatrix} \begin{Bmatrix} \boldsymbol{A}_1 \\ \boldsymbol{A}_2 \\ \boldsymbol{A}_3 \end{Bmatrix} + \begin{Bmatrix} \tilde{\boldsymbol{V}}_1 \\ 0 \\ 0 \end{Bmatrix} \Delta f \tag{8a}$$

or again in the simplified form as

$$\boldsymbol{K}\,\Delta\boldsymbol{A} = \tilde{\boldsymbol{f}} + \tilde{\boldsymbol{V}}\,\Delta f \tag{8b}$$

where the only difference with respect to equation (6b) is in the vector that multiplies Δf which is given as

$$\tilde{\boldsymbol{V}}_1 = \int_0^{2\pi} \left[\boldsymbol{C}^{\boldsymbol{T}} \cos(\tau) - 2\zeta\left(\frac{\Omega_0}{\omega_N}\right)\boldsymbol{C}^{\boldsymbol{T}} \sin(\tau) \right] \mathrm{d}\tau \tag{9}$$

where the excitation frequency is taken as a constant value, $\Omega_0 \to \Omega$. By using commercial software such as Wolfram Mathematica, the symbolic expression can be integrated into all matrices from equations (7) and (9) in an analytical form and later used for numerical calculations in the IHB and continuation code.

The IHB methodology is the solution procedure based on the following steps. First, we initialize the values of $\boldsymbol{A}_i$, Ω_0 or f_0 in equation (6b) or (8b) in such a manner that the tangent stiffness matrix $\boldsymbol{K}$ is not a singular matrix. Then by introducing the Newton-Raphson method to solve the obtained system of algebraic equations the equations (6b) and (8b)

iteratively. The results for increments given in vector $\Delta \boldsymbol{A}_i$ are obtained by solving the $\Delta \boldsymbol{A} = \boldsymbol{K}^{-1}\boldsymbol{R}$ in every iteration until the residue Euclidian norm $\|\boldsymbol{R}\|$ is smaller than a pre-set tolerance. The norm value of the residuum vector is adopted to be $\|\boldsymbol{R}\| \leq \epsilon$, where tolerance is adopted as $\epsilon = 10^{-9}$. Furthermore, the incremental vector $\Delta \boldsymbol{A}$ will be added to the vector of Fourier coefficients during the iterative process $\{\boldsymbol{A}_i\}^{p+1} = \{\boldsymbol{A}_i\}^{p} + \{\Delta \boldsymbol{A}_i\}^{p+1}$. The vector $\boldsymbol{A}$ tends to some finite value in every iteration for the fixed value of other parameters. This leads to a process where given displacements $x_{10}(\tau), x_{20}(\tau)$ and $I_0(\tau)$ tends to exact solutions when the corrective vector term $\boldsymbol{R}$ tends to zero.

The continuation method

The numerical continuation is a useful method in detecting the complex dynamic behaviors of many systems by showing the results in the form of response diagrams.[41] To trace frequency-amplitude and force-amplitude response curves, the combination of the continuation and IHB method proposed in Refs.[37–40] is employed. The numerical continuation used in this paper relies on the predictor-corrector methods available in the literature, with the solution procedure starting from an arbitrary initial vibration state. It is shown that the optimal starting point is a linear solution that is far away from the resonance state. However, for tracing the force-amplitude response curves, a small value of excitation force amplitude is a good starting position. This means that after initialization procedure, the tracing process will continue point – to – point calculation by using the $\Delta\Omega$ or Δf incremental processes to obtain the corresponding response curves, as given in Refs.[37–39] The main drawback of this process is that the incrementation procedure can fail if limit points (such as turning points) are encountered or the solution curve forms a loop (when the curve cuts itself). In that situations, the standard incrementation procedures obtained directly from the IHB methodology cannot form complete response curves. On the other hand, to trace frequency and force response

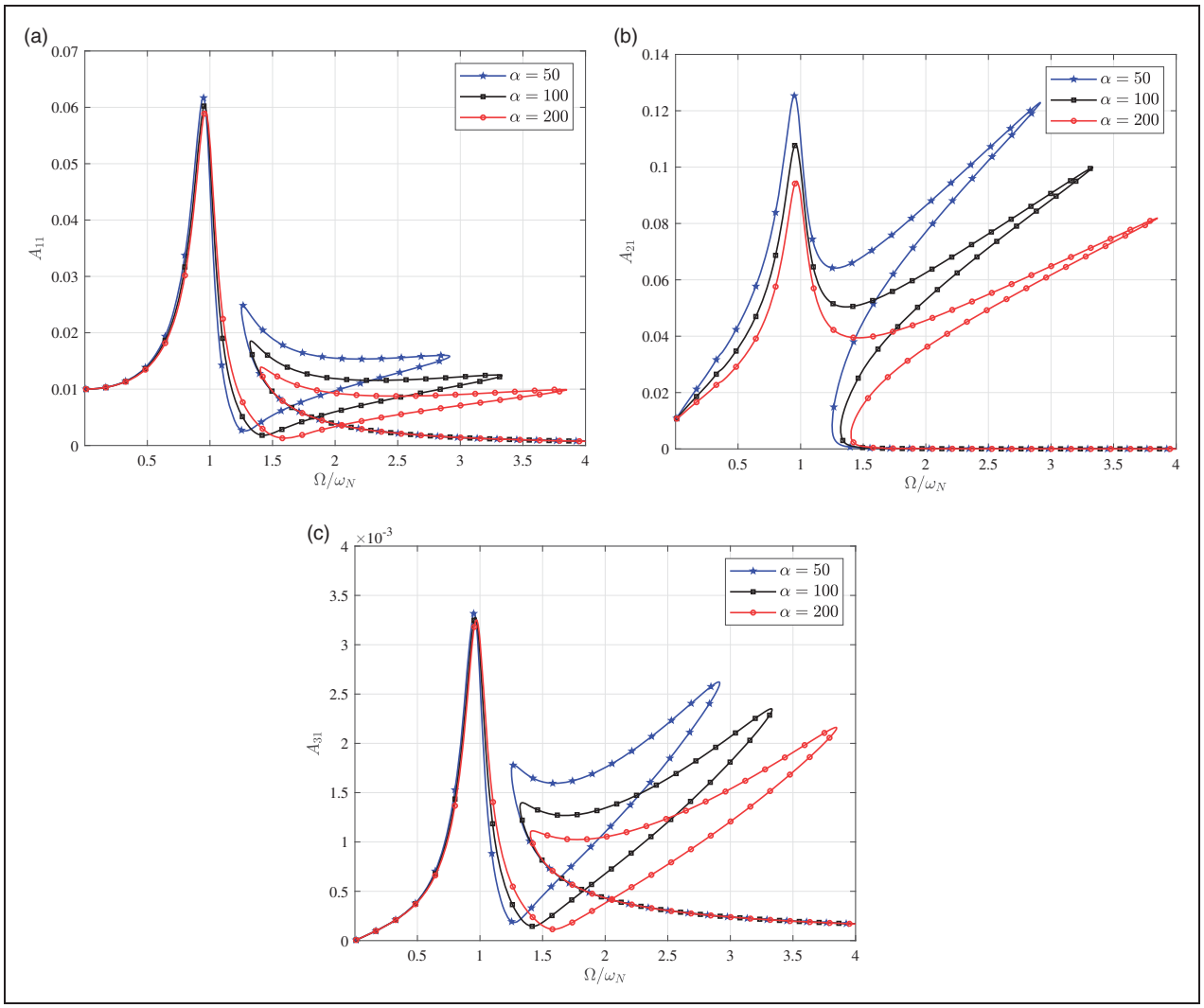

Figure 2. Frequency–amplitude response diagrams for different values of dimensionless stiffness parameter α

curves in the entire frequency or force amplitude range, and to eliminate failures due to critical points, one may use the arc-length continuation methodology based on the predictor-corrector method. In the following, we adopt this continuation procedure in the manner as proposed in Refs.[37,38]

The arc-length continuation method used for tracing the periodic response curves as a function of the excitation frequency, force or any other parameter is based on the following steps.[37,38] As a starting point for tracing the response curves by using the continuation method we need to determine initial solutions $(\boldsymbol{X}_{i-2},\ \boldsymbol{X}_{i-1})$ by the IHB method. Then, arc-length parameter η is introduced for finding a slope as

$$\boldsymbol{X}' = \frac{\boldsymbol{X}_{i-1} - \boldsymbol{X}_{i-2}}{\boldsymbol{X}_{i-1} - \boldsymbol{X}_{i-2}} \tag{10}$$

where $\boldsymbol{X}$ is the vector $\boldsymbol{X} = [\boldsymbol{A},\ \Omega]^{\boldsymbol{T}}$ or $\boldsymbol{X} = [\boldsymbol{A},\ f]^{\boldsymbol{T}}$ that depends on the corresponding response curve. Then, the first prediction solution of the next point $\boldsymbol{X}_i$ of the traced curve is formulated

$$\boldsymbol{X}_p = \boldsymbol{X}_{i-1} - \Delta\eta \boldsymbol{X}' \tag{11}$$

Next step is to determine a corrected solution by implementing the Newton-Raphson procedure, where the starting point is the first predicted solution of $\boldsymbol{X}_i$ on tracing response curve (i.e. $\boldsymbol{X}_p$). Therefore, extending the system given in equations (6a) or (8a) by an augmented equation

$$g(\boldsymbol{X}) - \eta = 0 \tag{12}$$

where such a system will be more appropriate to use in tracing the response curves.

Following the procedures are given in Refs.,[37,38,41] and adopting the quadratic form of the pseudo-arc-length method and function $g(\boldsymbol{X})$, where $g(\boldsymbol{X}) = \boldsymbol{X}^{\boldsymbol{T}}\boldsymbol{X}$, the incremental relation from equation (12) is given as

$$\frac{\partial g}{\partial \boldsymbol{A}^{\boldsymbol{T}}}\Delta\boldsymbol{A} + \frac{\partial g}{\partial \Omega}\Delta\Omega + g - \eta - \Delta\eta = 0 \tag{13}$$

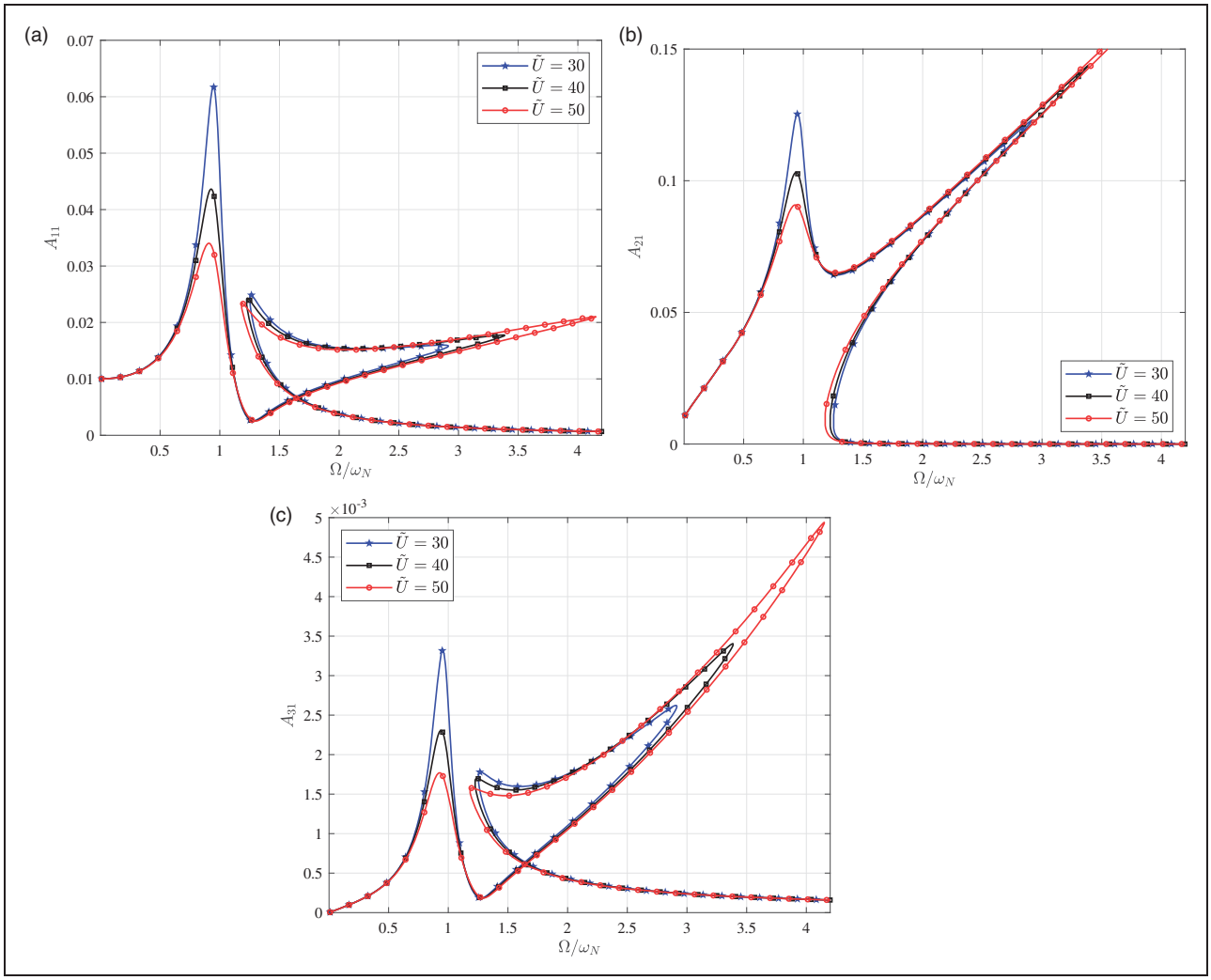

Figure 3. Frequency–amplitude response diagrams for different values of dimensionless flow speed $\tilde{U}$.

Using the extended system as a combination of equations (7a) and (7b), we get the following system of incremental equations for tracing the frequency-response curve

$$\begin{bmatrix} \boldsymbol{K}_{11} & \boldsymbol{K}_{12} & \boldsymbol{K}_{13} & -\tilde{\boldsymbol{V}}_1 \\ \boldsymbol{K}_{21} & \boldsymbol{K}_{22} & 0 & -\tilde{\boldsymbol{V}}_2 \\ \boldsymbol{K}_{31} & 0 & \boldsymbol{K}_{33} & -\tilde{\boldsymbol{V}}_3 \\ \left\{\frac{\partial g}{\partial \boldsymbol{A}_1}\right\}^T & \left\{\frac{\partial g}{\partial \boldsymbol{A}_2}\right\}^T & \left\{\frac{\partial g}{\partial \boldsymbol{A}_3}\right\}^T & \frac{\partial g}{\partial \Omega} \end{bmatrix} \begin{Bmatrix} \Delta \boldsymbol{A}_1 \\ \Delta \boldsymbol{A}_2 \\ \Delta \boldsymbol{A}_3 \\ \Delta \Omega \end{Bmatrix} = \begin{Bmatrix} \boldsymbol{R}_1 \\ \boldsymbol{R}_2 \\ \boldsymbol{R}_3 \\ \Delta\eta - g \end{Bmatrix} \tag{14}$$

where

$$\boldsymbol{R}_1 = \tilde{\boldsymbol{F}}_1 + \boldsymbol{R}_{11}\boldsymbol{A}_1 + \boldsymbol{R}_{12}\boldsymbol{A}_2 + \boldsymbol{R}_{13}\boldsymbol{A}_3$$

$$\boldsymbol{R}_2 = \boldsymbol{R}_{21}\boldsymbol{A}_1 + \boldsymbol{R}_{23}\boldsymbol{A}_3$$

$$\boldsymbol{R}_3 = \boldsymbol{R}_{31}\boldsymbol{A}_1 + \boldsymbol{R}_{33}\boldsymbol{A}_3.$$

Now, using equation (14) in the Newton-Raphson iterative procedure, the predicted solution can be determined in the whole range of response function. Moreover, the response includes critical or turning points and loops. For tracing the force-amplitude response curve, the same procedures can be employed by combining the equatiom (8a) and continuation technique with considering $\boldsymbol{X} = [\boldsymbol{A}, f]^{\boldsymbol{T}}$. As stated in Refs.,[37,38] in order to determine the next point on the response curve, the slope $\boldsymbol{X}'$ should be updated and η set to zero. The value of the $\Delta\eta$ parameter known as the arc-length increment represents an arbitrary step length and should be adopted in such a manner that the continuation process can trace the whole response curve without difficulties. By using the continuation approach for both, frequency-amplitude and force-amplitude curves, the stable and unstable branches of periodic solutions can be determined. However, the stability of a specific periodic solution is not investigated in this study.

Numerical results

The numerical study is performed to investigate effects of different material parameters on nonlinear

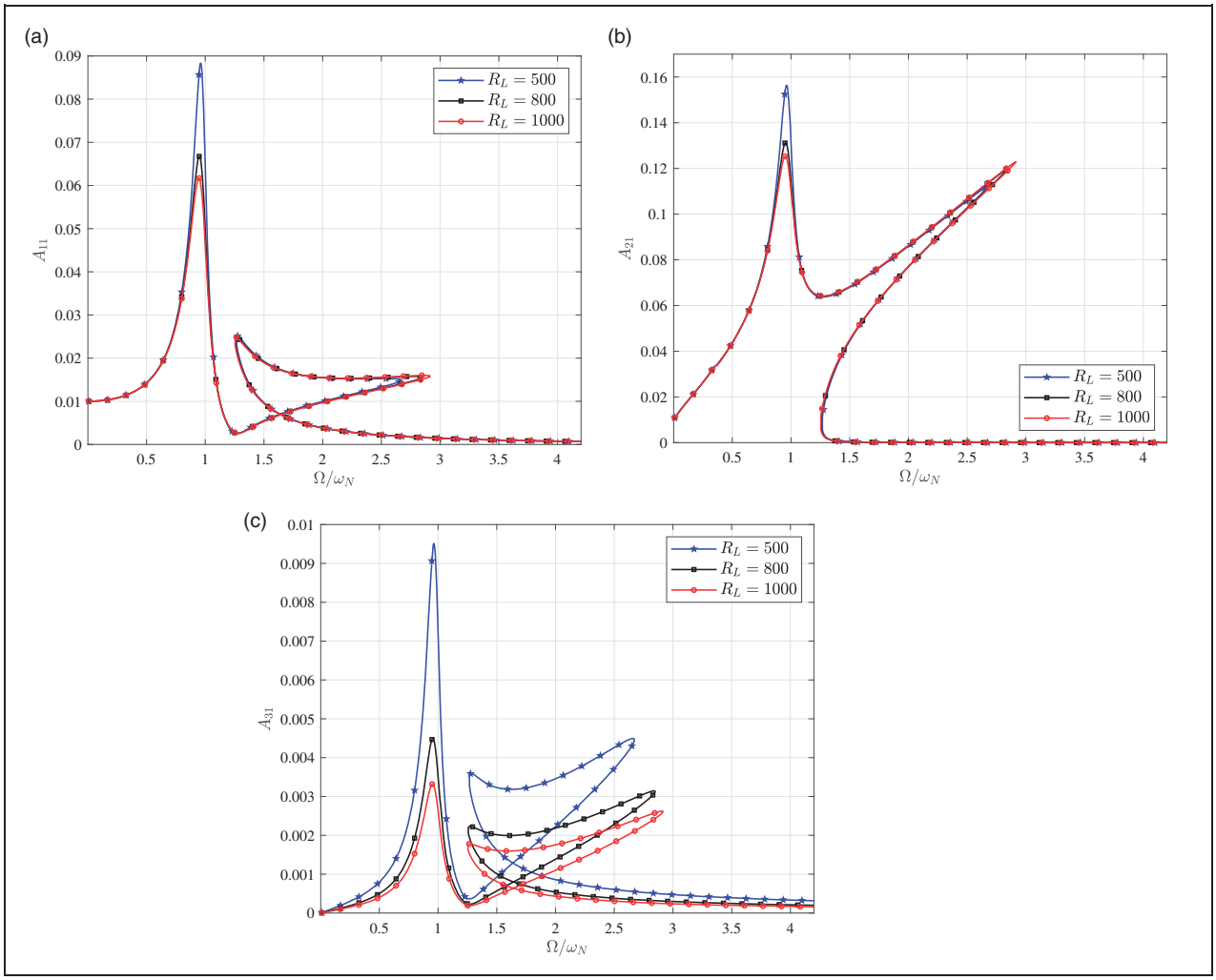

Figure 4. Frequency–amplitude response diagrams for different values of electrical load resistance $R_L(\Omega)$.

periodic responses of the electromagnetic EH with additional nonlinear oscillator subjected to base excitation and galloping oscillations by using the IHB and continuation methods. The IHB is very convenient to detect periodic orbits in a semi-analytical form, especially for the systems where nonlinearity is given in the polynomial form. Graphical representation of the nonlinear periodic responses of the proposed system is given in the form of response curves for different parameters such as excitation frequency and force amplitude. The effects of different values of nonlinear stiffness parameters, flow speed, and electrical load resistance are presented in the following response diagrams. It is shown that the dual-mass system is more efficient for energy harvesting purposes compared to the single mass system as stated in Vicente-Ludlam et al.[29] To estimate the average power of the proposed EH device, the time history diagrams are plotted for different values of nonlinear stiffness parameter and flow speed.

The physical characteristics of the primary structure i.e. a bluff-body and the electromagnetic EH model are adopted from Vicente-Ludlam et al.[10] For the internal nonlinear attachment, we adopted a dimensionless damping parameter $\beta = 0.005$ and the nonlinear stiffness as $\alpha = 50, 100, 200$. The mass ratio is adopted to be $\Gamma = 0.1$. For the solution process, we assume $N_h = 5$ odd terms in the Fourier series. It should be noted that all calculations and program codes are developed in the MATLAB environment.

Frequency and force responses of the proposed energy harvesting device

The effects of changing nonlinear stiffness parameter α of the additional nonlinear oscillator, flow speed $\tilde{U}$ and electrical load resistance R_L on frequency response diagrams are shown in Figures (2) to (4). One can observe that response amplitudes are increased for the freqency ratio Ω/ω_N in the range 0.1–4 with amplitudes of the primary structures A_{11}, nonlinear oscillator A_{21} and induced current A_{31} given on the ordinate axis. It should be noted that response amplitudes are defined as $A_{ij} = \sqrt{a_{ij} + b_{ij}}$, where the coefficients a_{ij} and b_{ij} are given in equation (5). The frequency response curves shown in Figure 2 are displaying nonlinear behaviour, where the first

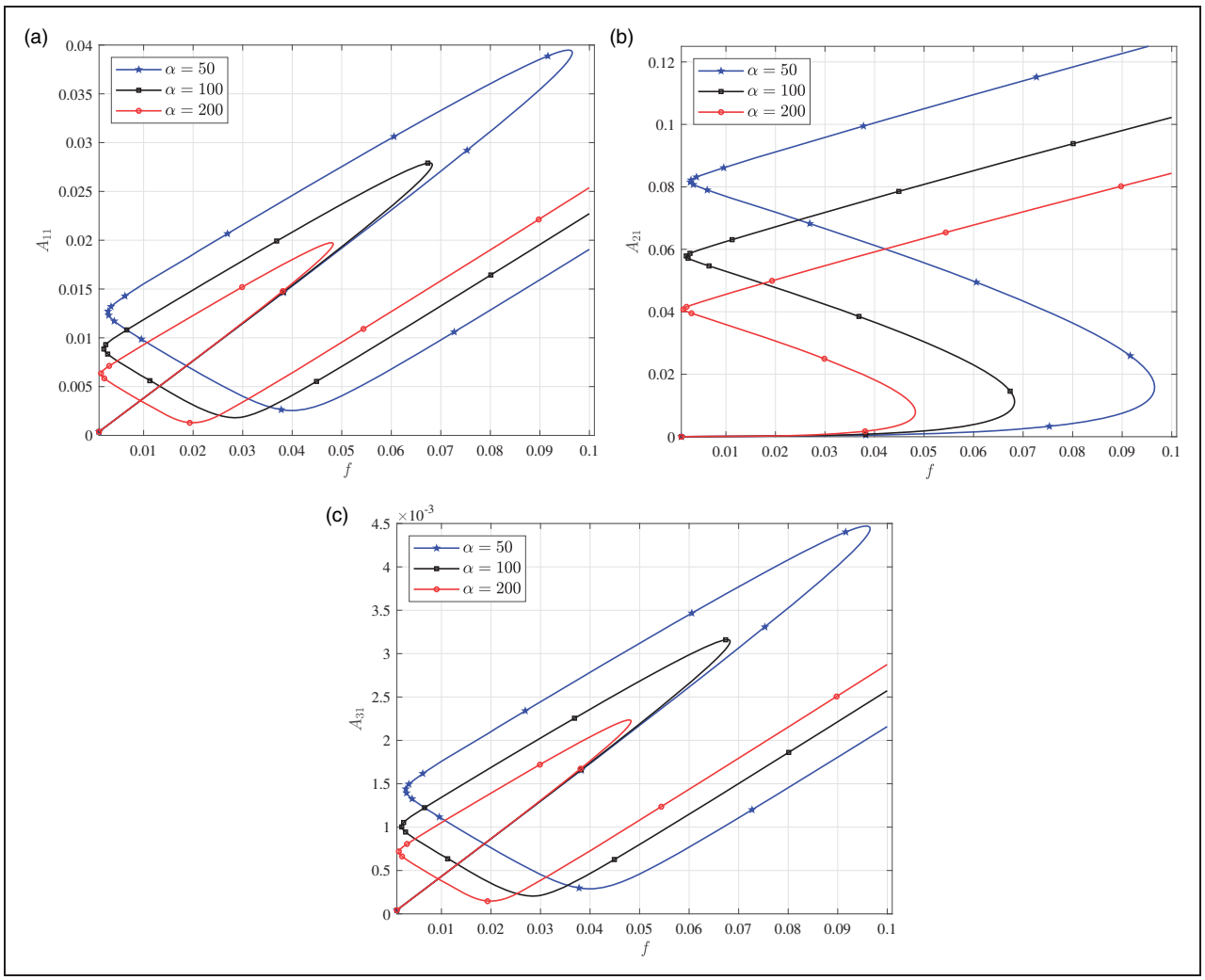

Figure 5. Force–amplitude response diagrams for different values of dimensionless stiffness parameter α.

one shows a loop type (Figure 2(a)) while the second one shows the hardening spring-type nonlinear behavior, which implies the jump phenomena (Figure 2(b)). The third curve forms a loop (Figure 2(c)) in a similar way as in the case of the first amplitude. All these nonlinear phenomena appears after reaching the linear resonance state, given as a peak amplitude on the response diagram. From the physical point of view, the reason for the appearance of these nonlinear effects is the introduction of the additional nonlinear oscillator in the system.

Starting from $\Omega/\omega_N = 0.1$, the response amplitude given in Figure 2(a) changes almost linearly when passing through the resonant state until the frequency ratio riches the value close to 1.7. At that point, the loop appears leading to the the appearance of region with multiple periodic solutions. Note that for a continuous increase of the frequency ratio far from the linear resonant state, the response amplitudes decreases until some finite values. Similar behavior can be observed in Figure 2(c). On the other hand, from Figure 2(b), it can be observed that for an increase of the frequency ratio to some higher values, the frequency response function passes through the resonant state and then the nonlinear hardening behavior appears with bending of the amplitude curve to the right-hand side. An increase of the frequency ratio value increases the frequency response curve that reaches its maximum and then jumps to some lower values. Further increase of the frequency ratio causes a decrease of amplitudes to some finite small values. The influence of an increase of the nonlinear stiffness parameter α causes a decrease of response amplitudes A_{ij} in the whole frequency range. However, this influence leads to the widening of the area with multiple periodic solutions as given in Figure 2. According to Malatkar and Nayfeh,[45] the formation of loops is caused by the coupling of two oscillators with nonlinear springs. Since amplitudes in the loop are larger than those outside the loop, such system can exibits better EH performance within the frequency range of the loop.

Figure 3 shows the frequency-response amplitude diagrams for A_{ij} and different values of the flow speed $\tilde{U} = 30, 40, 50$. The linear resonant state is

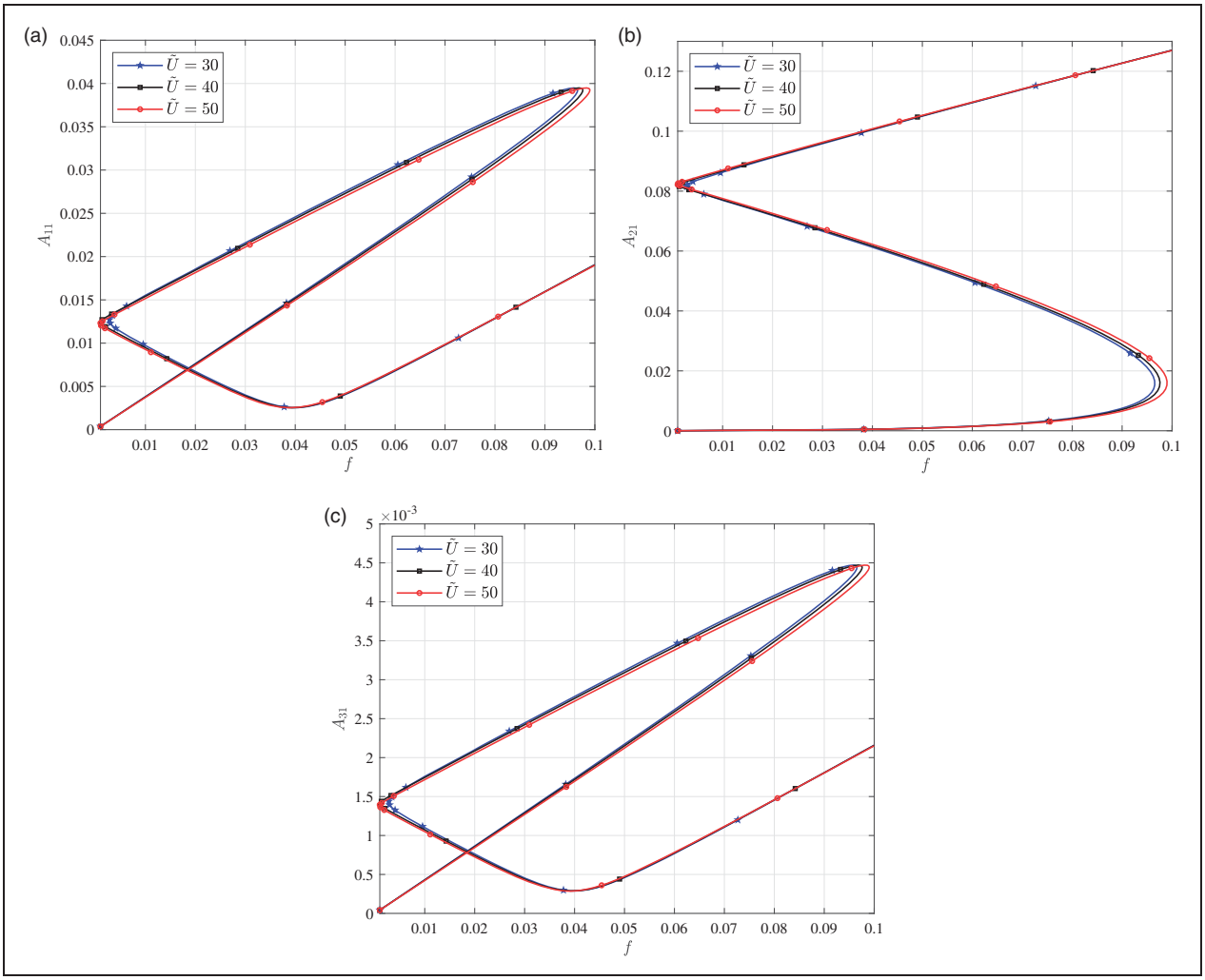

Figure 6. Force–amplitude response diagrams for different values of dimensionless flow speed $\tilde{U}$.

represented by the amplitude peak at the frequency ratio value around 0.9. Further increase of the frequency ratio causes appearance of the nonlinear phenomena such as loops (Figure 3(a) and (c)) and jumps (Figure 3(b)). One can notice that an increase of the flow speed leads to reduced response amplitudes near the first resonant regime. Furthermore, the effect on the nonlinear response become more prominent when the area with loops and hardening spring behavior is extended. Generally, the response amplitudes become higher for larger frequency ratios but after reaching some turning point they rapidly decrease to some lower values.

On the other hand, electrical resistance load R_L has a much larger effect on the response amplitudes, especially in the linear resonance state around the value of frequency ratio $\Omega/\omega_N = 0.9$. However, the effect of electrical resistance load is weakening and it is very small around the point where multiple periodic solutions appear, Figure 4(a). From Figure 4(b), it can be observed that an increase of the resistance load R_L leads to a decrease of the frequency-response amplitudes in the linear resonant regime but almost vanishes after the frequency ratio value 1.2, i.e. when the hardening effect appears. One can notice that the influence of electric resistance load leads to reduced response amplitudes A_{31}, especially in the area where loops appear, Figure 4(c).

It can be observed that the response amplitude A_{31} of the induced electrical current $I(\tau)$ has significantly higher amplitude in the case of an electromagnetic energy harvester device based on the dual-mass system. For the single-mass system, the response amplitude is formed only by one response amplitude peak in the narrow frequency range, as shown in Daqaq et al.[46] The extended dual-mass system shows hardening behaviour as a result of the strong positive cubic nonlinearity of additional nonlinear oscillator. This advantage of the dual mass system can be utilized in design procedures of more efficient EH devices subjected to fluid flow and base excitation.[10]

Figures 5 to 7 display the force-amplitude diagrams for different values of the nonlinear stiffness

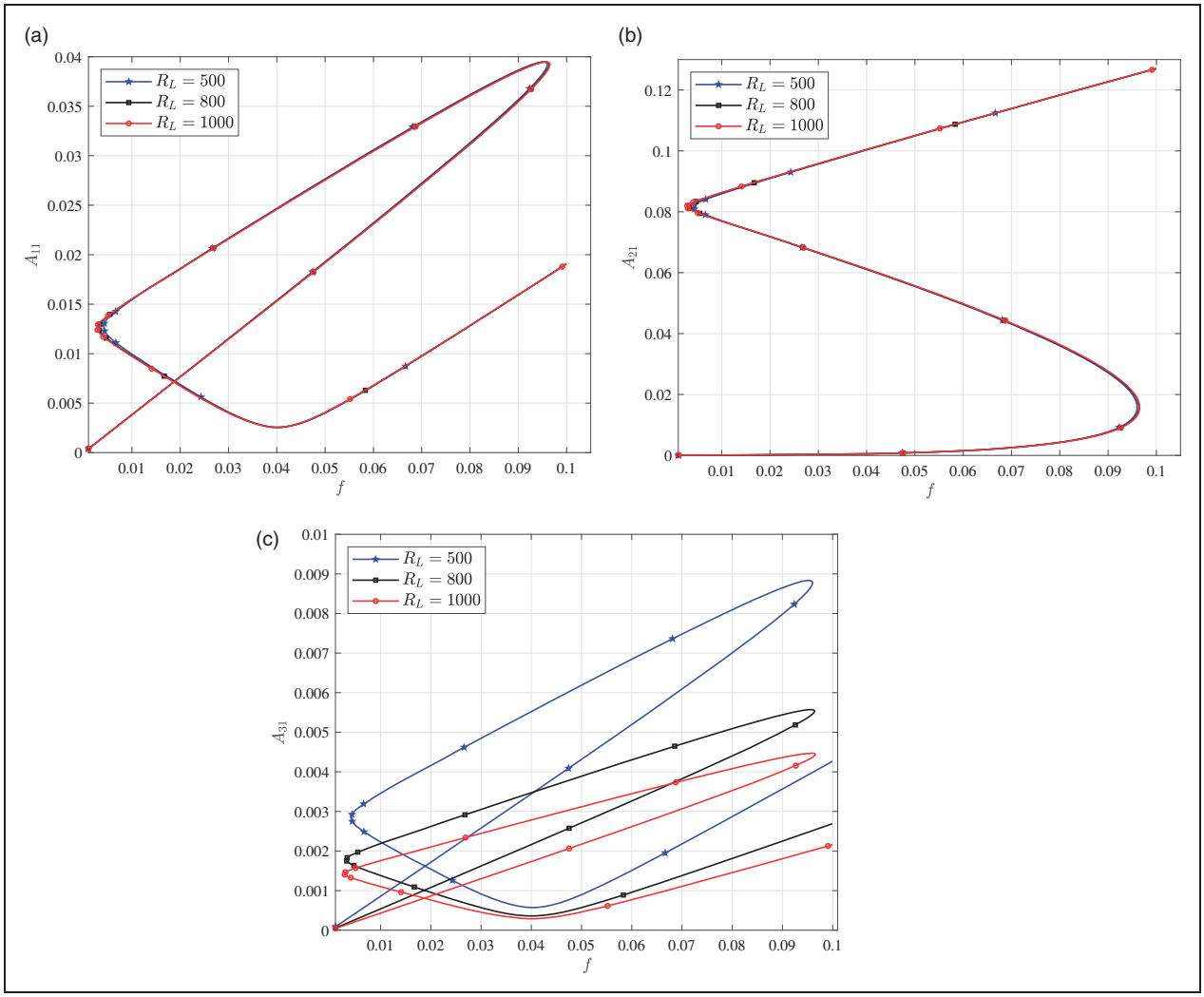

Figure 7. Force–amplitude response diagrams for different values of electrical load resistance $R_L(\Omega)$.

parameter α, speed flow $\tilde{U}$ and electrical load resistance R_L for the adopted value of the frequency ratio parameter $\Omega/\omega_N = 2$. By increasing the amplitude of base excitation f from some small value 10^{-3} to some finite value 10^{-1}, it can be noticed that response curves have totally different behavior comparing to the curves obtained for frequency responses. We can observe in Figure 5(a) that the response amplitude A_{11} forms a loop for all values of the nonlinear stiffness parameter in such a way that an increase of the parameter α leads to a decrease of response amplitudes. On the other hand, further increase of the amplitude of base excitation f causes an increase of A_{11} linearly but with lower amplitude than in the area where loops appear. Similar behavior of the response amplitude is recognized for A_{31} in Figure 5(c). However, response amplitude A_{21} representing the vibration amplitude of the additional nonlinear oscillator forms "circles" caused by jump effects. This nonlinear phenomenon significantly increases response amplitude for small range of amplitudes of base excitation f. It can be observed that the nonlinear stiffness parameter α reduces the response amplitude in the whole range of excitation amplitudes f as expected. Next figure shows the influence of flow speed $\tilde{U}$ on the force – amplitude response curves A_{11}, A_{21}, and A_{31}. It is clear that an increase of the flow speed $\tilde{U}$ is followed by a very small, almost invisible, cahnge of the force-response diagrams. These regions of multiple periodic solutions, caused by attaching the additional nonlinear oscillator inside the primary structure leads to higher vibration amplitudes as well as higher values of induced current. Figure 7 shows the influence of electrical resistance load R_L on the force-amplitude response curves. Starting from very low values of excitation amplitude f, further increase leads to the formation of loops (Figure 7(a) and (c)) and the appearance of jump phenomena (Figure 7(b)). These areas with multiple periodic orbits leads to higher vibration amplitudes of the dual-mass system. Moreover, the electrical load resistance R_L has the largest influence on the amplitude A_{31}, i.e. the amplitude of the induced current in the coil. As expected,[9] an increase of the values of electrical load resistance decreases the amplitude A_{31}.

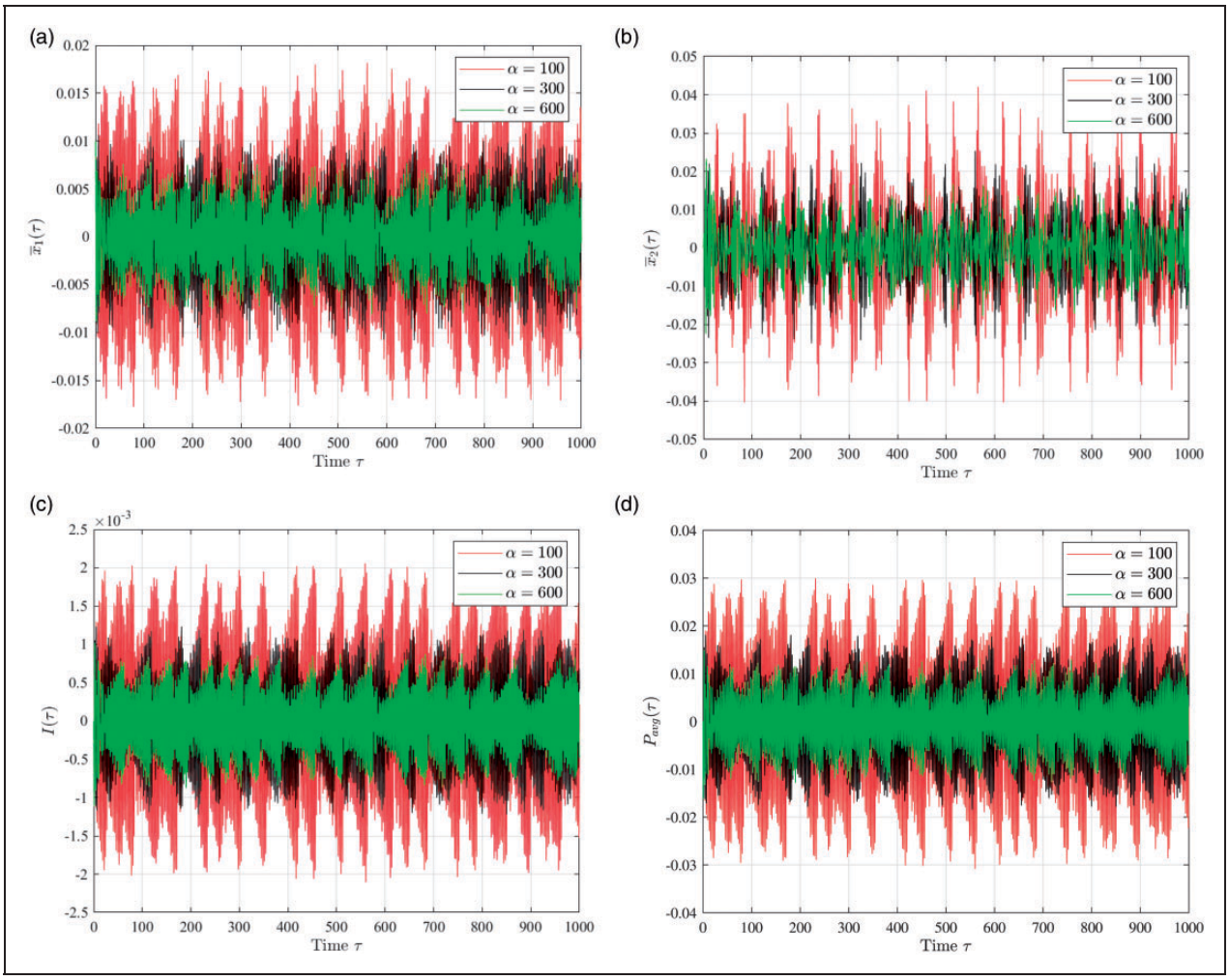

Figure 8. Time responses of dual-mass energy harvester for different values of the nonlinear spring stiffness α and fixed values of parameters: $R_L = 500(\Omega)$, $\bar{U} = 20$, $\xi = 10$, $f = 0.001$.

Time response of the proposed nonlinear dual-mass energy harvesting device

In order to analyse the performance of the proposed nonlinear dual-mass EH device and harvested power, the time responses for displacements $\bar{x}_1(\tau), \bar{x}_2(\tau)$, and output current $I(\tau)$ are plotted and investigated in this section. Moreover, in Dai et al.[23] formulation of the average harvested power is derived as $P_{avg} = \frac{1}{2} R_L i^2$ and presented in the form of time response diagrams. By using the direct numerical integration (ode45 in Matlab), system from equation (2) is solved for different values of the nonlinear stiffness parameter α and flow speed $\bar{U}$. From the physical viewpoint, these two parameters are directly related to the overall stiffness and damping of the presented system. For their optimal values, it is possible to set the system to work in such a way to achive best performance of the considered dual-mass based EH system. For better understanding of the energy harvesting performance and plotted time responses, the next initial conditions are adopted $\bar{x}_1(0) = 0.01, \bar{x}_2(0) = 0 = \dot{\bar{x}}_1(0) = \dot{\bar{x}}_2(0) = 0$ in each of the following numerical examples. Further, it should be noted that all the simulations are performed for the excitation frequency $\frac{\Omega}{\omega_N} = 0.5$. Figure 8 shows time responses of the first $\bar{x}_1(\tau)$ and the second $\bar{x}_2(\tau)$ displacement as well as the current $I(\tau)$ and average power P_{avg} of the EH device. The dimensionless time period is adopted as $T = 1000$ in all simulations.

To understand the effects of varying nonlinear stiffness parameter α and flow speed $\bar{U}$, time responses of the primary structure $\bar{x}_1(\tau)$ and the additional nonlinear oscillator $\bar{x}_2(\tau)$ are presented in Figures 8 and 9. One can observe that additional nonlinear spring on the primary structure increases the response amplitudes with respect to the linear case and thus having better performance as energy harvester. From the relation given in equation (2) it is obvious that an increase of the nonlinear stiffness parameter α decreases the values of response amplitudes and therefore decreases the average power of the system. This behaviour can be noticed in Figure 8(a) to (c), where the amplitudes of the primary structure $\bar{x}_1(\tau)$, nonlinear oscillator $\bar{x}_2(\tau)$ and output current $I(\tau)$ are reduced for an increase of the nonlinear stiffness α. At the same time, in

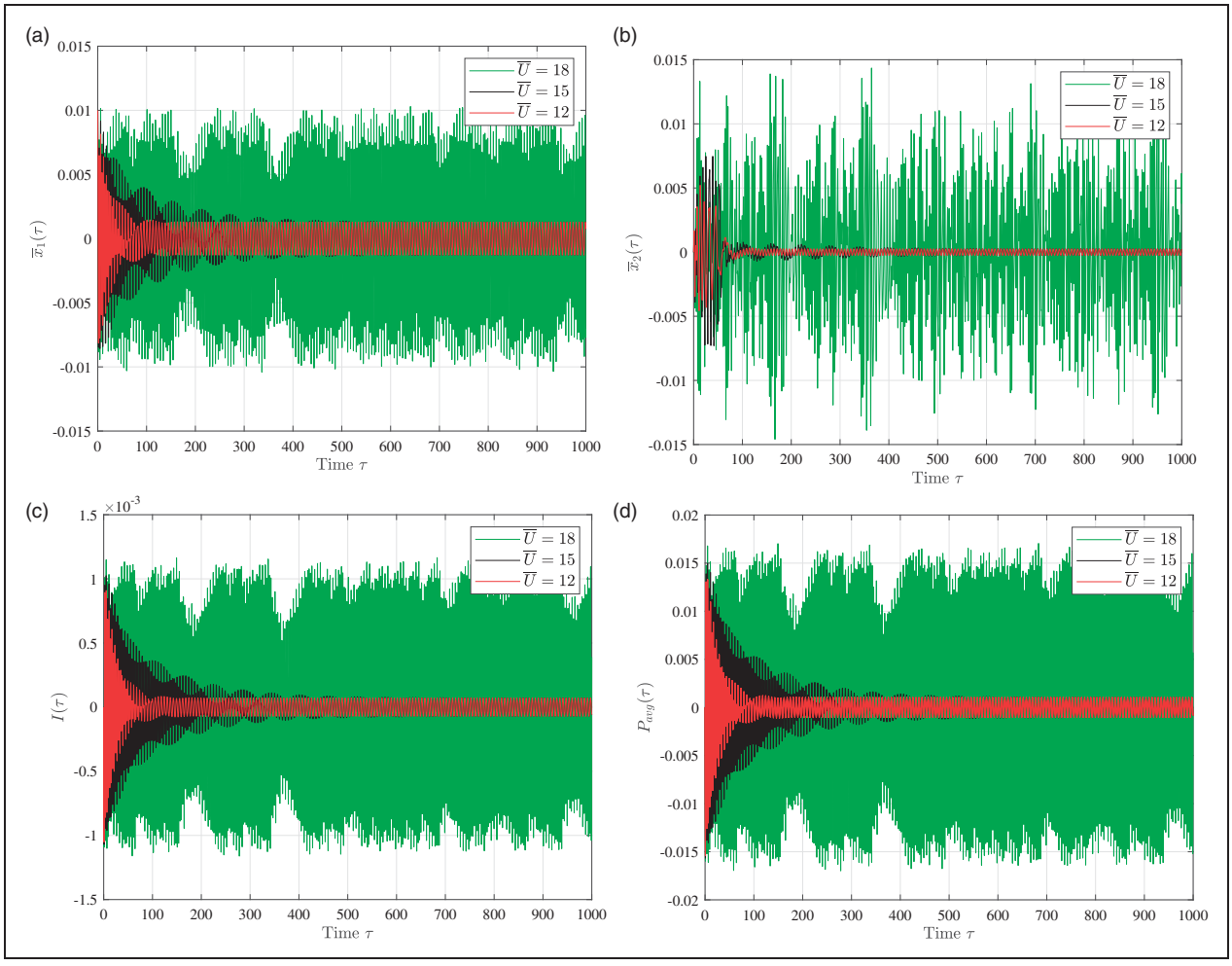

Figure 9. Time responses of dual-mass energy harvester for different values of the flow velocity $\bar{U}$ and fixed values of parameters: $R_L = 500(\Omega)$, $\alpha = 300$, $\xi = 10$, $f = 0.001$.

Figure 8(d) one can also observe a decrease of the average harvested power P_{avg} for an increase of the nonlinear stiffness α.

Further, significantly lower response amplitudes are obtained for low values of the flow speed. From Figure 9(a) and (b) one can observe that lower values of the flow speed yields smaller time response amplitudes of the primary structure $\bar{x}_1(\tau)$ and the additional nonlinear oscillator $\bar{x}_2(\tau)$, where system enters into the steady-state regime after some time with the amplitude of harmonic base excitation becoming dominant. Similar situation occurs for time response amplitudes of the output current $I(\tau)$ and the average harvested power P_{avg}, Figure 9(c) and (d). However, for the highest presented value of the flow speed $\bar{U} = 18$ system responses becomes bounded and chaotic. This behaviour might be attributed to the combined effect of the nonlinearities such as the cubic spring nonlinearity with nonlinear galloping force F_U and harmonic base excitation. Because of this unpredictable behaviour, one should be careful in design procedures of EH devices with combined nonlinearities in order to avoid unstable performance of the device. On the other side, higher values of the flow speed can lead to higher values of the average harvested power P_{avg} of dual-mass EH system, as shown in Figure 9(d).

Conclusions

The nonlinear periodic response of an electromagnetic vibration energy harvester with an additional nonlinear oscillator subjected to the external base excitation and fluid flow is studied. For tracing the branches of periodic responses, a combination of the incremental harmonic balance and continuation methods is applied to the system of nonlinear differential equations of motion. The influence of different model parameters such as the nonlinear stiffness, speed of fluid flow, and electrical load resistance on the frequency and force response diagrams is studied in detail. Increased efficiency of the dual-mass energy harvester compared to an eqivalent single-mass energy harvester system is demonstrated. As the main result of this paper, it is shown that the introduction of the nonlinear attachment into the primary structure causes the appearance of multiple periodic solutions, which leads to wider frequency range with higher response amplitudes and therefore to higher harvested power of the device. However, time response diagrams demonstrated a significant effect of the nonlinear stiffness and flow speed on average harvested power. Based on aforementioned, this study can be used in future design procedures of more efficient energy harvester devices based on electromagnetic principle and subjected to combined excitations.

Acknowledgements

This paper is a contribution in honour of the 75th birthday and 50 years of scientific work of Professor Katica (Stevanović) Hedrih.

Declaration of Conflicting Interests

The author(s) declared no potential conflicts of interest with respect to the research, authorship, and/or publication of this article.

Funding

The author(s) disclosed receipt of the following financial support for the research, authorship, and/or publication of this article: This study was funded by the Marie Skłodowska-Curie Actions - European Commission fellowship (grant number 799201- METACTIVE) and the Serbian Ministry of Education, Science and Technological Development through Mathematical Institute of the Serbian Academy of Sciences and Arts.

References

1. Nakamura T, Kaneko S, Inada F, et al. (eds) *Flow-induced vibrations: classifications and lessons from practical experiences*. Butterworth-Heinemann, 2013.
2. Li D, Wu Y, Da Ronch A, et al. Energy harvesting by means of flow-induced vibrations on aerospace vehicles. *Progr Aerosp Sci* 2016; 86: 28–62.
3. Abdelkefi A. Aeroelastic energy harvesting: a review. *Int J Eng Sci* 2016; 100: 112–135.
4. Abdelkefi A, Hajj MR and Nayfeh AH. Piezoelectric energy harvesting from transverse galloping of bluff bodies. *Smart Mater Struct* 2013; 22: 015014.
5. Abdelkefi A, Yan Z and Hajj MR. Modeling and nonlinear analysis of piezoelectric energy harvesting from transverse galloping. *Smart Mater Struct* 2013; 22: 025016.
6. Abdelkefi A, Hajj MR and Nayfeh AH. Phenomena and modeling of piezoelectric energy harvesting from freely oscillating cylinders. *Nonlinear Dyn* 2012; 70: 1377–1388.
7. Dai HL, Abdelmoula H, Abdelkefi A, et al. Towards control of cross-flow-induced vibrations based on energy harvesting. *Nonlinear Dyn* 2017; 88: 2329–2346.
8. Dai HL, Abdelkefi A and Wang L. Piezoelectric energy harvesting from concurrent vortex-induced vibrations and base excitations. *Nonlinear Dyn* 2014; 77: 967–981.
9. Dai HL, Abdelkefi A, Javed U, et al. Modeling and performance of electromagnetic energy harvesting from galloping oscillations. *Smart Mater Struct* 2015; 24: 045012.
10. Vicente-Ludlam D, Barrero-Gil A and Velazquez A. Optimal electromagnetic energy extraction from transverse galloping. *J Fluids Struct* 2014; 51: 281–291.
11. Dai HL, Yang YW, Abdelkefi A, et al. Nonlinear analysis and characteristics of inductive galloping energy harvesters. *Commun Nonlinear Sci Numer Simul* 2018; 59: 580–591.
12. Pennisi G, Mann BP, Naclerio N, et al. Design and experimental study of a nonlinear energy sink coupled to an electromagnetic energy harvester. *J Sound Vibr* 2018; 437: 340–357.
13. Liu H and Gao X. Vibration energy harvesting under concurrent base and flow excitations with internal resonance. *Nonlinear Dyn* 2019; 96: 1067–1081.
14. De Marqui C Jr and Erturk A. Electroaeroelastic analysis of airfoil-based wind energy harvesting using

piezoelectric transduction and electromagnetic induction. *J Intell Mater Syst Struct* 2013; 24: 846–854.
15. Dias JAC, De Marqui C Jr and Erturk A. Three-degree-of-freedom hybrid piezoelectric-inductive aeroelastic energy harvester exploiting a control surface. *AIAA J* 2015; 53: 394–404.
16. Bibo A and Daqaq MF. Energy harvesting under combined aerodynamic and base excitations. *J Sound Vibr* 2013; 332: 5086–5102.
17. Daqaq MF, Bibo A, Akhtar I, et al. Micropower generation using cross-flow instabilities: a review of the literature and its implications. *J Vibr Acoust* 2019; 141: 030801.
18. Vakakis AF, Gendelman OV, Bergman LA, et al. *Nonlinear targeted energy transfer in mechanical and structural systems* (vol. 156). New York: Springer Science & Business Media, 2008.
19. Vakakis AF. Passive nonlinear targeted energy transfer. *Phil Trans R Soc A* 2018; 376: 20170132.
20. Gendelman O, Manevitch LI, Vakakis AF, et al. Energy pumping in nonlinear mechanical oscillators: part I—dynamics of the underlying Hamiltonian systems. *J Appl Mech* 2001; 68: 34–41.
21. Tumkur RKR, Domany E, Gendelman OV, et al. Reduced-order model for laminar vortex-induced vibration of a rigid circular cylinder with an internal nonlinear absorber. *Commun Nonlinear Sci Numer Simul* 2013; 18: 1916–1930.
22. Blanchard A, Bergman LA and Vakakis AF. Vortex-induced vibration of a linearly sprung cylinder with an internal rotational nonlinear energy sink in turbulent flow. *Nonlinear Dyn* 2020; 99: 593–517.
23. Dai HL, Abdelkefi A and Wang L. Usefulness of passive non-linear energy sinks in controlling galloping vibrations. *I J Nonlinear Mech* 2016; 81: 83–94.
24. Dai HL, Abdelkefi A and Wang L. Vortex-induced vibrations mitigation through a nonlinear energy sink. *Commun Nonlinear Sci Numer Simul* 2017; 42: 22–36.
25. Zhang Y, Tang L and Liu K. Piezoelectric energy harvesting with a nonlinear energy sink. *J Intell Mater Syst Struct* 2017; 28: 307–322.
26. Kremer D and Liu K. A nonlinear energy sink with an energy harvester: transient responses. *J Sound Vibr* 2014; 333: 4859–4880.
27. Tang X and Zuo L. Enhanced vibration energy harvesting using dual-mass systems. *J Sound Vibr* 2011; 330: 5199–5209.
28. Nishi Y. Power extraction from vortex-induced vibration of dual mass system. *J Sound Vibr* 2013; 332: 199–212.
29. Vicente-Ludlam D, Barrero-Gil A and Velazquez A. Enhanced mechanical energy extraction from transverse galloping using a dual mass system. *J Sound Vibr* 2015; 339: 290–303.
30. Javed U, Abdelkefi A and Akhtar I. An improved stability characterization for aeroelastic energy harvesting applications. *Commun Nonlinear Sci Numer Simul* 2016; 36: 252–265.
31. Blevins RD. *Flow-induced vibration*. Van Nostrand Reinhold. New York, 1990.
32. El-Hami M, Glynne-Jones P, White NM, et al. Design and fabrication of a new vibration-based electromechanical power generator. *Sens Actuat A Phys* 2001; 92: 335–342.
33. Dou S and Jensen JS. Optimization of nonlinear structural resonance using the incremental harmonic balance method. *J Sound Vibr* 2015; 334: 239–254.
34. Fu YM, Zhang J and Bi RG. Analysis of the nonlinear dynamic stability for an electrically actuated viscoelastic microbeam. *Microsyst Technol* 2009; 15: 763–769.
35. Kong X, Li H and Wu C. Dynamics of 1-dof and 2-dof energy sink with geometrically nonlinear damping: application to vibration suppression. *Nonlinear Dyn* 2018; 91: 733–754.
36. Zhou S, Song G, Li Y, et al. Dynamic and steady analysis of a 2-DOF vehicle system by modified incremental harmonic balance method. *Nonlinear Dyn* 2019; 98: 75–94.
37. Leung AYT and Chui SK. Non-linear vibration of coupled duffing oscillators by an improved incremental harmonic balance method. *J Sound Vibr* 1995; 181: 619–633.
38. Bhattiprolu U, Bajaj AK and Davies P. Periodic response predictions of beams on nonlinear and viscoelastic unilateral foundations using incremental harmonic balance method. *Int J Solids Struct* 2016; 99: 28–39.
39. Huang JL, Su RKL, Lee YY, et al. Nonlinear vibration of a curved beam under uniform base harmonic excitation with quadratic and cubic nonlinearities. *J Sound Vibr* 2011; 330: 5151–5164.
40. Wang S, Hua L, Yang C, et al. Applications of incremental harmonic balance method combined with equivalent piecewise linearization on vibrations of nonlinear stiffness systems. *J Sound Vibr* 2019; 441: 111–125.
41. Seydel R. 2009. *Practical bifurcation and stability analysis* (vol. 5). New York: Springer Science & Business Media.
42. Noll MU, Lentz L and von Wagner U. On the discretization of a bistable cantilever beam with application to energy harvesting. *FU Mech Eng* 2019; 17: 125–139.
43. Noll MU, Lentz L and von Wagner U. On the improved modeling of the magnetoelastic force in a vibrational energy harvesting system. *Journal of Vibration Engineering & Technologies* 2020; 8: 285–295.
44. Wang DA and Chang KH. Electromagnetic energy harvesting from flow-induced vibration. *Microelectron J* 2010; 41: 356–364.
45. Malatkar P and Nayfeh AH. Steady-state dynamics of a linear structure weakly coupled to an essentially nonlinear oscillator. *Nonlinear Dyn* 2006; 47: 167–179.
46. Daqaq MF, Masana R, Erturk A, et al. On the role of nonlinearities in vibratory energy harvesting: a critical review and discussion. *Appl Mech Rev* 2014; 66